# *Nucleation and Growth of $WSe_2$: Enabling Large Grain Transition Metal Dichalcogenides*

**UT Dallas Author(s):**

Ruoyu Yue, Yifan Nie, Lee A. Walsh,
Rafik Addou, Chaoping Liang, Ning Lu,
Adam T. Barton, Hui Zhu, Zifan Che,
Diego Barrera, Lanxia Cheng, Yves J. Chabal,
Julia W. P. Hsu, Jiyoung Kim, Moon J. Kim,
Robert M. Wallace, Kyeongjae Cho, Christopher L. Hinkle



**Citation:**

Yue, Ruoyu, Yifan Nie, Lee A. Walsh, Rafik Addou, et al. 2017. "Nucleation and growth of $WSe_2$: enabling large grain transition metal dichalcogenides." 2d Materials 4, doi:10.1088/2053-1583/aa8ab5

2D Materials

OPEN ACCESS

RECEIVED
7 July 2017

REVISED
23 August 2017

ACCEPTED FOR PUBLICATION
6 September 2017

PUBLISHED
22 September 2017



PAPER

# Nucleation and growth of $WSe_2$: enabling large grain transition metal dichalcogenides

Ruoyu Yue[1,4], Yifan Nie[1,4], Lee A Walsh[1], Rafik Addou[1], Chaoping Liang[1], Ning Lu[1], Adam T Barton[1], Hui Zhu[1], Zifan Che[1], Diego Barrera[1], Lanxia Cheng[1], Pil-Ryung Cha[2], Yves J Chabal[1], Julia W P Hsu[1], Jiyoung Kim[1], Moon J Kim[1], Luigi Colombo[3], Robert M Wallace[1], Kyeongjae Cho[1] and Christopher L Hinkle[1]

[1] Department of Materials Science and Engineering, University of Texas at Dallas, Richardson, TX 75080, United States of America
[2] School of Advanced Materials, Kookmin University, Jeongneung-gil 77, Seongbuk-gu, Seoul, 136-702, Republic of Korea
[3] Texas Instruments, Dallas, TX 75243, United States of America
[4] These authors have contributed equally to this work.

**E-mail:** chris.hinkle@utdallas.edu

**Keywords:** tungsten diselenide, transition metal dichalcogenides, van der Waals epitaxy, nucleation and growth, kinetic Monte Carlo simulation

Supplementary material for this article is available online

## Abstract

The limited grain size (<200 nm) for transition metal dichalcogenides (TMDs) grown by molecular beam epitaxy (MBE) reported in the literature thus far is unsuitable for high-performance device applications. In this work, the fundamental nucleation and growth behavior of $WSe_2$ is investigated through a detailed experimental design combined with on-lattice, diffusion-based first principles kinetic modeling to enable large area TMD growth. A three-stage adsorption-diffusion-attachment mechanism is identified and the adatom stage is revealed to play a significant role in the nucleation behavior. To limit the nucleation density and promote 2D layered growth, it is necessary to have a low metal flux in conjunction with an elevated substrate temperature. At the same time, providing a Se-rich environment further limits the formation of W-rich nuclei which suppresses vertical growth and promotes 2D growth. The fundamental understanding gained through this investigation has enabled an increase of over one order of magnitude in grain size for $WSe_2$ thus far, and provides valuable insight into improving the growth of other TMD compounds by MBE and other growth techniques such as chemical vapor deposition (CVD).

## 1. Introduction

The limited grain size (<200 nm) for transition metal dichalcogenides (TMDs) grown by molecular beam epitaxy (MBE) reported in the literature thus far is unsuitable for high-performance device applications [1–15]. Most of these results exhibit films with almost full surface coverage consisting of these small grains, indicating a high density of nucleation and grain boundary formation in the film. In this work, the fundamental nucleation and growth mechanism of $WSe_2$ is investigated through a detailed experimental design combined with first-principles kinetic modeling. The fundamental understanding gained through this investigation has enabled an increase of over one order of magnitude in grain size. This study focuses on $WSe_2$ but can also be extended to improve the growth of other TMD compounds and is applicable to other growth techniques in addition to MBE.

TMDs are two-dimensional (2D) layered materials that have attracted great attention due to their relatively inert surfaces and remarkable thickness-dependent electrical and optical properties [16–21]. For semiconducting TMDs like $MoS_2$ and $WSe_2$, an indirect to direct bandgap transition occurs as the film thickness is reduced from multilayer to monolayer due to quantum confinement [22–24]. Furthermore, the lack of covalent bonding between adjacent TMD layers enables heterostructure fabrication with a relaxed lattice matching criteria, allowing the stacking of materials based primarily on their electronic properties and quantum mechanical effects [25–29]. Among these materials, $WSe_2$ is one of the most interesting TMDs for a variety of devices due to its attractive electronic properties such as valley coherence for valleytronics, large band spin splitting for spintronics, and low carrier effective mass with suitable band alignment for broken-gap tunnel field-effect transistor (FET) applications [25, 30–32].

The majority of $WSe_2$-based devices reported in the literature to date have used exfoliated geological $WSe_2$ [33–36]. However, the geological TMD crystals, along with those produced by chemical vapor transport (CVT), have been shown to have a high density of structural defects, high impurity levels, and a large degree of variability across the same sample surface [37–40]. MBE is a promising growth method for TMDs, and heterostructures thereof, due to the potential of enhanced quality provided by a combination of high purity elemental sources and growth in an ultra-high vacuum (UHV) system. TMD materials such as $HfSe_2$, $SnSe_2$, $WSe_2$, $MoTe_2$, and $WTe_2$ have been grown by MBE with promising microstructure [2–7, 11–13, 21]. Like in those prior reports, we observe here rotational alignment between the $WSe_2$ layer and van der Waals substrates such as graphite, $Bi_2Se_3$, and $MoS_2$, and the absence of strain and misfit dislocations.

To facilitate device quality films with larger grains, we combine experimental MBE growth with an on-lattice, diffusion-based first principles kinetic Monte Carlo (KMC) model, which enabled the identification of a three-stage adsorption-diffusion-attachment mechanism. It is shown that the adatom stage plays a significant role in the nucleation behavior. The complex competition between kinetic factors including adsorption, desorption, on-substrate diffusion, attachment, and edge diffusion, which control different aspects of growth, has a significant influence on grain size.

## 2. Methods

van der Waals epitaxy was performed in a VG Semicon V80H MBE system using elemental sources (an effusion cell for selenium and an e-beam evaporator for tungsten) with a base pressure of $\sim 3 \times 10^{-10}$ mbar and a background pressure of $\sim 1 \times 10^{-9}$ mbar during growth. The growth chamber is equipped with an *in situ* reflection high-energy electron diffraction (RHEED) system to monitor crystal quality during growth. A systematic study of the impact of W and Se flux, substrate temperature, and their co-interaction was performed by systematically varying each of these parameters. The substrate temperatures investigated for $WSe_2$ growth were between 350 °C and 550 °C, the W flux was varied from $2 \times 10^{-9}$ mbar to $1 \times 10^{-8}$ mbar, and the Se flux range was between $1 \times 10^{-7}$ mbar and $1 \times 10^{-6}$ mbar. The detailed parameter settings for each experiment can be found in the supporting information table S1 (stacks.iop.org/TDM/4/045019/mmedia).

The substrate for the majority of the $WSe_2$ growth presented here was highly oriented pyrolytic graphite (HOPG) with a size of $12 \times 12\,mm^2$. Other substrates studied include *c*-plane (0 0 0 1) sapphire and MBE-grown $Bi_2Se_3$ on sapphire. As $Bi_2Se_3$ has a maximum thermal budget of 320 °C before chalcogen loss and sapphire is a non-van der Waals substrate, a direct comparison of the $WSe_2$ growth on the various substrates is not included in this work. Instead, we focus on the nucleation and growth on HOPG, a van der Waals substrate with high thermal stability. Detailed sample preparation steps are described in the supporting information.

Cross-sectional transmission electron microscopy (TEM) samples were made by FIB-SEM Nova 200 with a lift-out method. A JEM-ARM200F transmission electron microscope operated at 200 kV with probe aberration corrector was used for $WSe_2$ cross-section imaging.

The surface structure of the $WSe_2$ was examined in a separate UHV chamber (base pressure $\sim 1 \times 10^{-10}$ mbar) using an Omicron variable-temperature scanning tunneling microscope described in detail elsewhere [41]. The scanning tunneling microscopy (STM) image was obtained under constant current mode at room temperature, without any thermal treatment prior to imaging. The images were processed using WSxM software [42]. The *I–V* spectra were obtained from an average of 10 curves.

Atomic-force microscopy (AFM) measurements were carried out using a Veeco Model 3100 Dimension V atomic probe microscope with a silicon tip. More details about the AFM spatial resolution can be found in the supporting information.

The KMC simulation model includes adsorption, desorption, and atom hopping within the lattice sites of the bulk TMD. The hopping rates follow transition state theory, in the form of the Arrhenius relation. The adsorption energies and diffusion barriers are calculated from density functional theory (DFT) by VASP coupled by the nudged elastic band theory [43–47] which are then used as inputs into the KMC simulations. Random numbers are generated to select the proceeding events. For further details of the simulation, please refer to reference [48].

## 3. Results and discussion

### 3.1. Observed properties confirming high-quality $WSe_2$ growth by van der Waals epitaxy

HOPG was chosen as the substrate material for the majority of this study due to its inert 2D surface and thermal stability at elevated substrate temperatures. The high resolution STM image ($9 \times 9\,nm^2$) of monolayer $WSe_2$ grown on HOPG shown in figure 1(a) reveals the hexagonal moiré pattern (highlighted by blue dots) due to the lattice mismatch between $WSe_2$ and graphite. The measured periodic spacing from the moiré pattern (~9.8 Å) agrees well with the expected superposition between HOPG and unstrained $WSe_2$ with zero rotation angle at the interface [14]. This unstrained growth and rotational alignment are important characteristics of van der Waals epitaxy. Scanning tunneling spectroscopy (STS) spectra of monolayer and bilayer $WSe_2$ from the same sample (height line profile in the supporting information)

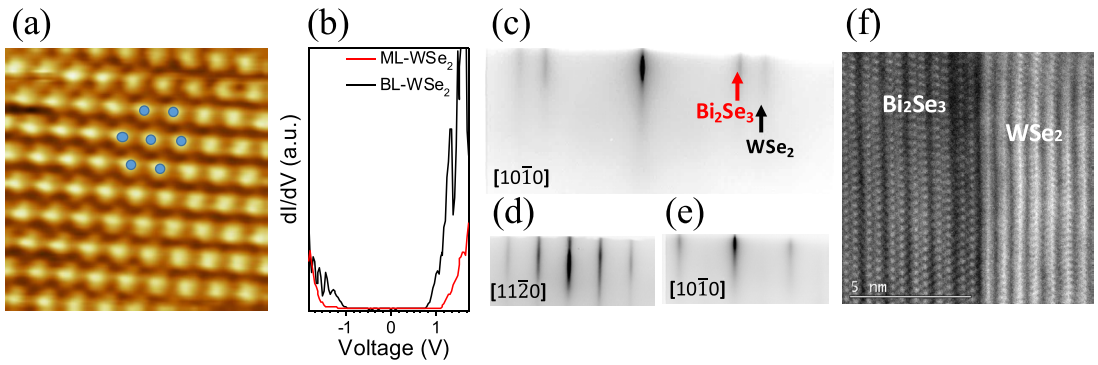


**Figure 1.** (a) STM ($9 \times 9\,\text{nm}^2$, $V_b = 0.14\,\text{V}$, $I_t = 1.2\,\text{nA}$) image of monolayer $WSe_2$ on HOPG shows the moiré pattern that indicates unstrained $WSe_2$ rotationally aligned to the substrate, (b) STS analysis ($V_b = 2\,\text{V}$, $I_t = 0.3\,\text{nA}$) of mono- and bi-layer $WSe_2$ grown on HOPG, showing the bandgap transition, (c)–(e) RHEED patterns of $WSe_2$ growth on a single crystal $Bi_2Se_3$ substrate: for sub-monolayer $WSe_2$ (c) and for full $WSe_2$ coverage (d) and (e), confirming rotational alignment to the substrate, (f) TEM image of a multilayered $WSe_2$ film grown on $Bi_2Se_3$ showing the layered structure and atomically abrupt interface with no evidence of misfit dislocations.

are shown in figure 1(b) and demonstrate the decrease in bandgap as the film thickness is increased from monolayer (2.6 eV) to bilayer (1.8 eV).

One issue with HOPG is its highly textured nature, where, even though there is out-of-plane alignment, there is in-plane rotational misorientation between different grains (see further discussion of this wire texturing of HOPG in the supporting information). This makes it difficult to determine the rotational alignment between the growing TMD layer and the HOPG substrate by diffraction techniques. The confirmation of rotational alignment between the $WSe_2$ and the substrate was enabled by using single-crystal $Bi_2Se_3$, another van der Waals material, as the substrate. *In situ* RHEED of $WSe_2$ grown on the $Bi_2Se_3$ is shown in figures 1(c)–(e). When the $WSe_2$ partially covers the $Bi_2Se_3$ surface, two different sets of RHEED streaks in the $[1\,0\,\bar{1}\,0]$ direction corresponding to the reciprocal lattice of both $WSe_2$ and $Bi_2Se_3$ are observed (figure 1(c)). The simultaneous appearance of streaks from both the substrate and $WSe_2$ indicates that the grown $WSe_2$ is rotationally aligned to the substrate, consistent with the observation of zero rotation angle between the growing $WSe_2$ and the substrate as shown in the moiré pattern from the STM image in figure 1(a). The extracted in-plane lattice constant ($a = 3.29\,\text{Å} \pm 0.03\,\text{Å}$) from the RHEED pattern, and confirmed by the STM measurement of 3.28 Å, is consistent with other reports [49]. When the substrate is fully covered, a single set of RHEED patterns appear in the $[1\,0\,\bar{1}\,0]$ and $[1\,1\,\bar{2}\,0]$ directions, corresponding to the reciprocal lattice of $WSe_2$ that is fully azimuthally aligned to the substrate (figures 1(d) and (e)). Similar rotational alignment has previously been observed in other epitaxially grown TMDs [1, 4, 8, 29, 50–52]. The corresponding cross-sectional TEM image of the $WSe_2$/$Bi_2Se_3$ heterostructure is presented in figure 1(f). The interface and crystalline properties of $WSe_2$ on $Bi_2Se_3$ are very similar to the growth on HOPG as shown in the supporting information (figure S3). The layered structure of the $WSe_2$ is evident and an atomically abrupt interface between the $WSe_2$ and $Bi_2Se_3$ is observed, with the complete absence of misfit dislocations despite a 21% lattice mismatch, further confirming the unstrained growth. The interlayer distance of the $WSe_2$ is measured to be 6.4 Å, consistent with the inter-planar spacing of $WSe_2$ crystals [53]. Further characterization, including x-ray photoelectron spectroscopy (XPS), Raman spectroscopy, and out-of-plane x-ray diffraction (XRD), in conjunction with the experimentally determined band alignment can be found in the supporting information to demonstrate high-quality $WSe_2$ crystalline films grown by MBE on all van der Waals substrates.

### 3.2. Novel growth modes in 2D materials and grain boundary reduction

The characterization results presented above show that $WSe_2$ grows unstrained and with its own lattice constant, indicating that lattice mismatch is not a significant factor in growing high-quality TMD films, as expected. However, the lattice mismatch results in the formation of grain boundaries as illustrated in figure 2(a). The distance between nucleation sites on a lattice-mismatched substrate is statistically unlikely to be an integer multiple of the $WSe_2$ lattice constant due to the different lattice spacing of the substrate and TMD material. As a result, incomplete unit cells form when the rotationally aligned grains merge together [54]. These grain boundaries are, of course, expected to degrade carrier mobility [55–57]. The density of grain boundaries increases for samples with a high nucleation density. Therefore, reducing the nucleation density is critical to achieving higher quality films. In this paper, we investigate the nucleation and growth mechanism to minimize the formation of these grain boundaries and thus achieve large area unstrained grains.

Attempts have been made to categorize TMD growth using traditional growth modes for three-dimensional (3D) materials, namely the Volmer–Weber, Stranski–Kranstanov, and Frank–van der

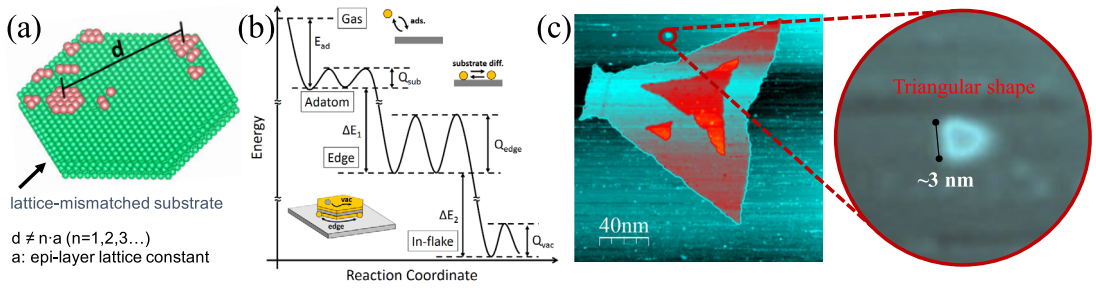


**Figure 2.** (a) Illustration of grain boundary formation due to lattice mismatch in van der Waals epitaxy, (b) reaction energy diagram of the growth process employed in the simulations, (c) STM image of the smallest triangular $WSe_2$ nucleus of 3.0 ± 0.3 nm grain size, comparable with KMC simulation result of 1.63 ± 0.21 nm.

Merwe modes [58]. These growth modes are generalized based on surface tension comparisons between the deposited film and the substrate [59]. However, the traditional categorization for the 3D materials is also based on the implicit assumption that the out-of-plane interaction of the material under deposition is comparable with the in-plane interaction, thus the aforementioned terms are interchangeable with the surface tension within the context of 3D materials. For 3D films, a strong interatomic interaction leads to both a strong surface tension and a strong out-of-plain interaction, the latter of which allows strain to be accumulated as the atomic layers grow [59]. However, the results presented in this work demonstrate that such reasoning does not apply to van der Waals material systems where the in-plane interaction is dominant over both of the out-of-plane interactions (epilayer–substrate and epilayer–epilayer). The dangling-bond-free surface of the ideal TMD crystal can, in theory, avoid vertical island growth (coarsening) and allows a thickness controlled layer-by-layer growth scenario [48]. Moreover, these traditional growth mode models are predominantly based on equilibrium thermodynamics and provide no information on crucial kinetic issues such as diffusion and nucleation. In fact, many observations suggest that under most experimental growth conditions, TMD growth strongly deviates from equilibrium. Imperfect structures such as grains with fractal morphology and unusual nuclei formation are observed in previous studies and later in this work [8]. These deviations from the ideal occur due to kinetic factors including adsorption, desorption, on-substrate diffusion, attachment, and edge diffusion. The lack of an existing applicable growth mechanism and an inadequate description of kinetic processes illustrate the need to combine experiment with a kinetic model to describe not only the thermodynamic relations, but also the atomic scale events. Combining an MBE experimental parameter study with on-lattice diffusion based KMC simulations provides the necessary insight to achieve larger grains and 2D growth.

### 3.3. Kinetics and thermodynamics of nucleus formation and critical nucleus size

To begin the consideration of TMD nucleation and growth by MBE, a three-stage model is proposed:

$$\text{Gas} \underset{\text{desorption}}{\overset{\text{adsorption}}{\rightleftarrows}} \underset{\text{(self-diffusion)}}{\text{Adatoms}} \overset{\text{attachment}}{\rightleftarrows} \underset{\text{(self-diffusion)}}{\text{Flake}}, \quad (1)$$

with the reaction energy diagram shown in figure 2(b) [60]. In this study, only atomic precursors are included, since the strong binding energy of clusters of the metal or chalcogen requires an overly high activation energy (5.44 eV for W-dimers and 4.64 eV for Se dimers) to participate in the epitaxial process [61, 62]. Atoms arriving at the substrate surface, rather than being reflected back into the ambient, have a probability of being adsorbed on the surface. The adsorbed atoms become adatoms and have a certain lifetime with diffusion occurring on the substrate surface. This stage of adatom diffusion on the substrate surface plays a pivotal role in nucleus creation and in the growth of an existing nucleus. A homogeneous nucleation requires that several adatoms arrive at the same spot via random substrate diffusion, which is improbable and requires a high local density of adatoms. The Gibbs free energy calculation can be expressed as $G = \frac{4\pi}{3} r^3 G_\nu + 4\pi r^2 \gamma$ for spherical nuclei or $G = \frac{\sqrt{3}}{4} a^2 G_A + 3a\gamma$ for planar triangular nuclei, where $G_\nu$ is the Gibbs volume energy, $G_A$ is the Gibbs area energy, and $\gamma$ is the interfacial energy or edge energy for 2D domains [63]. Although the $WSe_2$ nuclei shape highly depends on the growth conditions, which will be discussed later, both cases indicate that only a spherical nucleus with $r$ greater than the critical size $r_c = -\frac{2\gamma}{G_\nu}$, or a planar domain with edge $a$ greater than the critical size $a_c = -\frac{4\sqrt{3}\gamma}{G_A}$ is stable. The Gibbs and interfacial/edge energies for TMDs are not well established to date, making it difficult to deduce the critical cluster size analytically. From the KMC simulations, we are able to determine that a critical nucleus of $WSe_2$ takes the form of $W_{15\pm1}Se_{28\pm3}$ with a size of 1.63 ± 0.21 nm within the

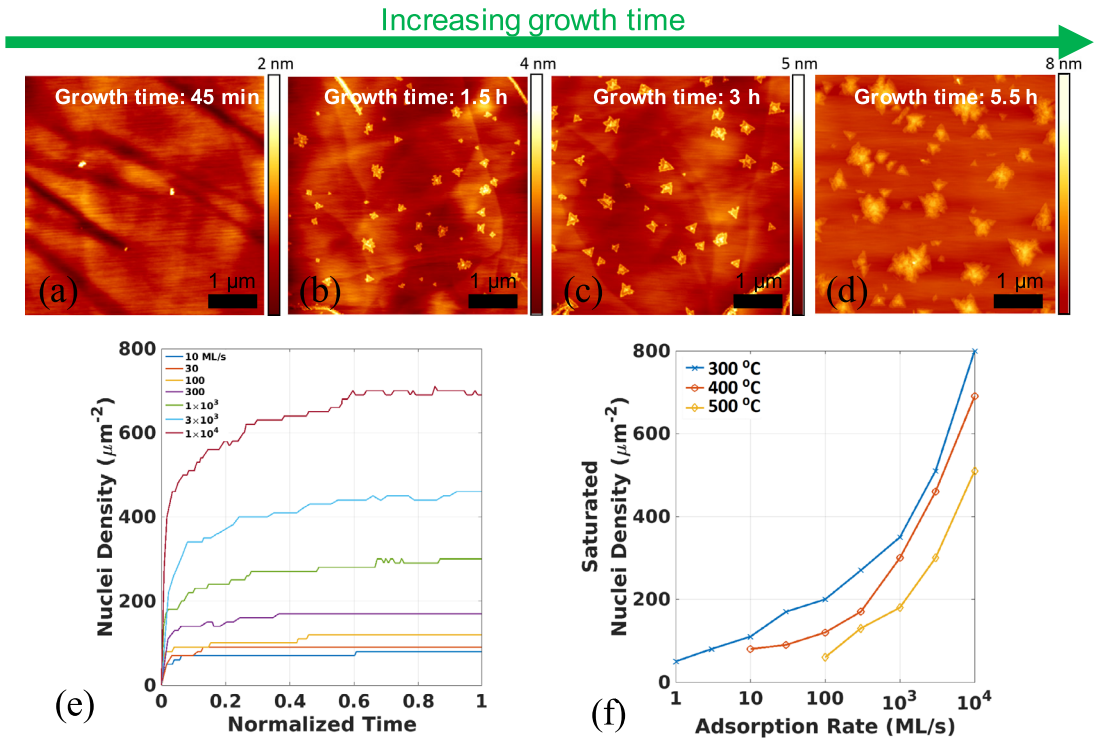


**Figure 3.** (a)–(d) AFM images that show how nucleation density increases rapidly during the low coverage stage and becomes stable after reaching ~15% coverage, (e) simulated homogeneous $WSe_2$ nuclei desnity as a function of normalized time under different adsorption rates at 400 °C with the chalcogen-to-metal ratio equal to 2.0, (f) simulated saturated nuclei density as a function of adsorption rate for different substrate temperatures. The growth conditions for figures (a)–(d) include: W flux of $5 \times 10^{-9}$ mbar, Se flux of $7 \times 10^{-7}$ mbar, and substrate temperature of 500 °C.

temperature range from 400 to 800 °C (see supporting information for details). While we expect the critical nucleus size to be temperature dependent, the change in the critical nucleus size within this temperature range is negligible (within the error bars of the critical nucleus size in our calculations). Experimentally, the smallest triangular $WSe_2$ nucleus observed from STM for 15 different spots (scan range of $100 \times 100\,nm^2$) across the sample is $3.0 \pm 0.3$ nm (figure 2(c)) and we observe a non-triangular nucleus of $2.5 \pm 0.3$ nm. After a stable nucleus is formed, it can capture incoming adatoms that approach the nucleus via on-substrate diffusion.

### 3.4. Suppressing nuclei and grain boundary formation rate

As shown in figures 3(a)–(d), the rate of nuclei formation during the initial stages is high, followed by a subsequent slowing down of the nuclei formation rate. A similar trend has also been observed in the MBE growth of other materials [59, 64]. This is a sign of the competition between nucleation and adatom attachment and suggests the necessity to include the adatom kinetics to our understanding. In the temperature range studied here, the diffusion length of the adatoms exceeds the average adatom–adatom and adatom–nucleus distance. Therefore, when the nuclei density increases to a level comparable to the surface adatom density, it becomes favorable for the adatoms to attach to an existing nucleus rather than to form a new one, and thus the formation of new nuclei ceases and existing nuclei grow in size [64].

Similar to the experimental observations, the simulation results in figure 3(e) confirm that the formation rate of new nuclei decreases as the nuclei density increases, reaching the saturated nuclei density before the surface coverage reaches 10%. In addition, the saturated nucleation density in figure 3(f) shows a strong dependence on both the substrate temperature and the flux which motivates further experimental investigation of these growth parameters.

The impact of substrate temperature is shown in figures 4(a)–(c), where increasing the substrate temperature reduces the growth rate and nucleation density. The underlying reason is due to the increased desorption rate at elevated temperature, consistent with the results from simulation (figure 3(f)). The W flux also has a large impact on the nucleation and growth rates (figures 4(d)–(f)). Decreasing the W flux from $1 \times 10^{-8}$ mbar to $2 \times 10^{-9}$ mbar results in a dramatic decrease in the density of nuclei, with almost no nuclei observed after 1.5 h growth time for W fluxes lower than $2 \times 10^{-9}$ mbar. These results are consistent with the KMC simulations shown in figure 3(f), i.e. that the nuclei count decreases with decreasing adsorption rate, which is proportional to the flux. With both reduced substrate temperature and higher W flux, it is reasonable to expect a higher surface adatom density, and a corresponding exponential increase in nucleation density indicates

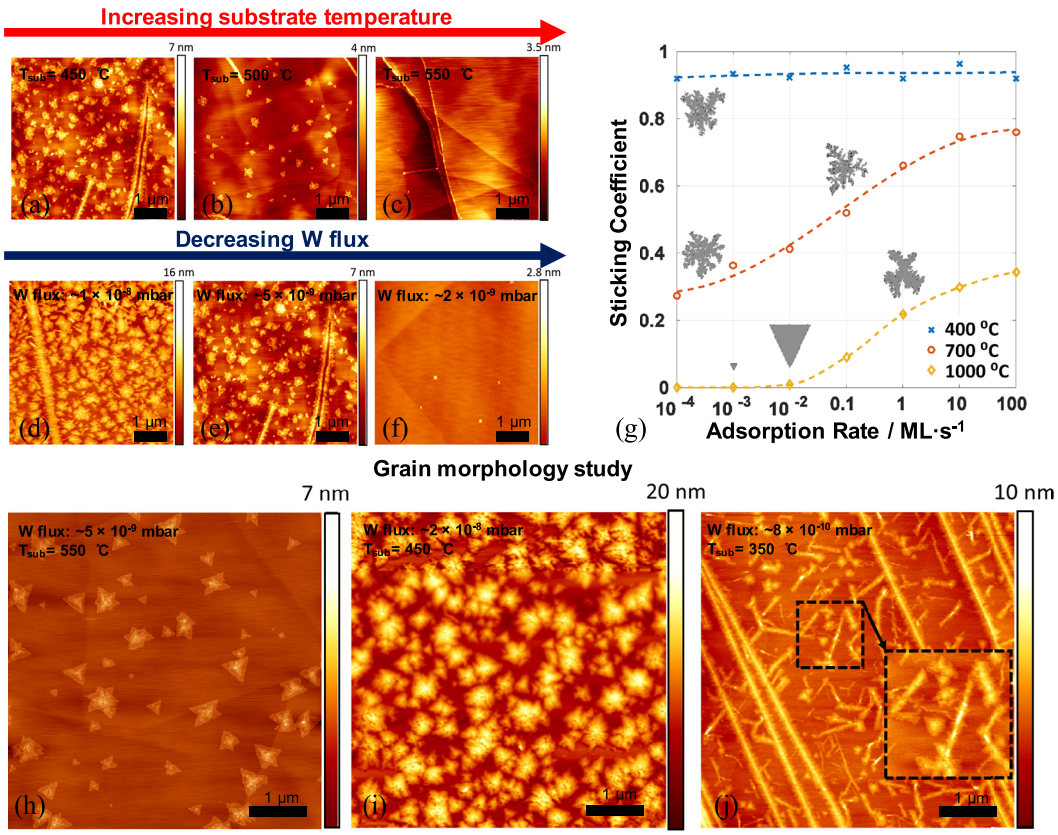


**Figure 4.** AFM images showing the impact of substrate temperature ((a)–(c)) and W flux ((d)–(f)) in limiting nucleation density, (g) the simulated sticking coefficient, as a function of the adsorption rate, for three different substrate temperatures, inserted are the corresponding domain morphology images obtained during simulation, (h)–(j) AFM images of the various grain morphologies observed indicating that low substrate temperature or high W flux will lead to non-compact, discontinuous growth. The apparent non-alignment of grains shown in (h) are caused by the wire-textured HOPG substrate (see supporting information for more details).

a close relationship between the adatom density and stable nuclei formation [59].

### 3.5. Sticking coefficient dependence on temperature and nucleus composition

The percentage of precursor that results in stable domains, commonly referred to as the sticking coefficient ($S_c$), is a product of two conversion factors corresponding to the two-step reaction illustrated in equation (1): (1) the percentage of atoms incident upon the surface which become adatoms, and (2) the percentage of adatoms which result in stable domains. The estimated sticking coefficient of W atoms drops from about 16% to 4.1% when the substrate temperature is elevated from 450 °C to 525 °C (the method used for this approximation is described in the supporting information). These low sticking coefficients, which are consistent with the KMC simulations, confirm that a significant fraction of adatoms do not make it past the adsorption–desorption step in equation (1), and so do not contribute to deposition. There is almost no $WSe_2$ growth at 550 °C during the 1.5 h growth time, suggesting a further reduction in the sticking coefficient and an enhanced desorption rate due to the elevated substrate temperature. The sticking coefficient of Se atoms is considerably lower than that for W and is dependent on the chemical environment. For a substrate temperature of 450 °C, the calculated Se $S_c$ values are ~0.13% for a W flux of $5 \times 10^{-9}$ mbar (figure 4(e)) and ~0.36% for a W flux of $1 \times 10^{-8}$ mbar (figure 4(d)). Thus, the sticking coefficients are dependent on the chemical environment, a common observation in the epitaxy of compound crystals [65–67], where different elements depend on each other to form the desired crystal structure.

According to first principles DFT calculations, the absolute value of the adsorption energy (1.49 eV for W and 0.65 eV for Se), which dictates the desorption rate, is over an order of magnitude higher than the diffusion energy barrier (0.03 eV for W and 0.06 eV for Se) [60]. Since desorption is negligible at low temperature, most of the adatoms are able to form stable domains that exceed the critical nucleus size. However, the desorption rate increases exponentially at elevated substrate temperature due to the Arrhenius nature of the process ($r = D_0 e^{-\frac{\Delta G^{\neq}}{k_B T}}$, where $D_0$, $\Delta G^{\neq}$, $k_B$ and $T$ correspond to the pre-exponential coefficient, activation energy, Boltzmann constant and temperature, respectively). More adatoms desorb from the surface at these elevated temperatures before forming stable nuclei, reducing the adatom density and sticking coefficient. Therefore, simulation and experimental results point

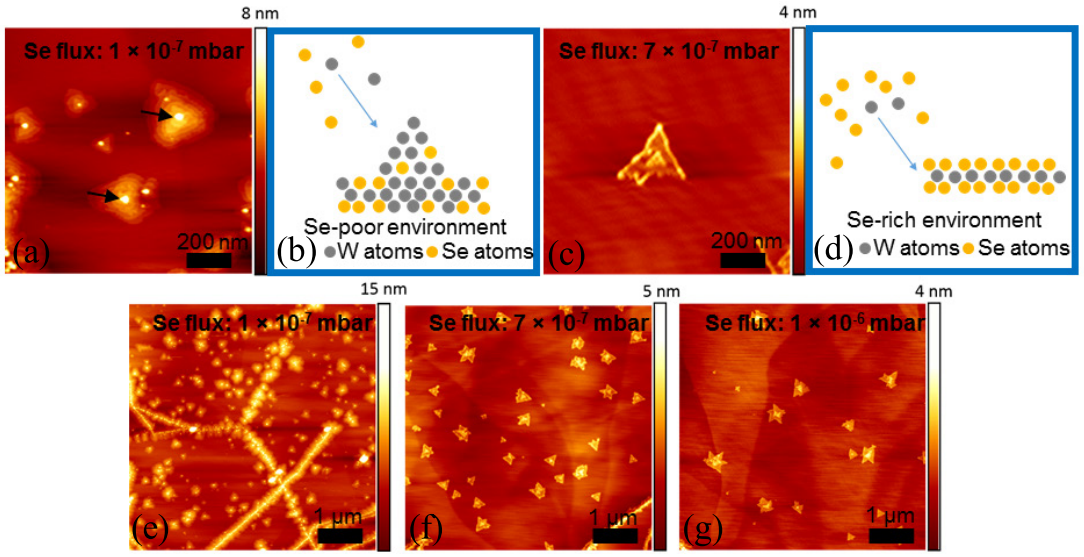


**Figure 5.** (a)–(d) AFM images and illustrations showing the impact of Se flux in suppressing vertical growth. Island growth occurs in a Se deficient environment due to W-rich nucleus formation while more 2D growth is achieved in a Se-rich environment, (e)–(g) Se flux also impacts the $WSe_2$ nucleation density where higher Se flux again limits W-rich nuclei. Each of these growths utilized a W flux of $5 \times 10^{-9}$ mbar, substrate temperature of 500 °C, and growth time of 3 h.

to the use of higher substrate temperatures and smaller W fluxes to reduce the nucleation density by reducing the adatom density.

### 3.6. Compact versus fractal grain morphology

The morphology of the growing grains is another important aspect in the ability to predict the quality of TMD films. Compact domains with triangular shape are observed under conditions of low growth rate in figures 4(g) and (h) (achieved by low W flux together with high substrate temperature), while discontinuous domains are observed when the growth rate is increased (figures 4(g) and (i)). The randomly branched, highly discontinued shapes are referred to as fractals. This triangular-fractal transition is the result of the competition between adatom attachment and edge diffusion processes; the latter being responsible for the relaxation of the domain from the initial shape (often random and branching) to the thermodynamically favorable configuration (compact triangle for the TMD monolayers) [68]. DFT simulations have shown that the edge diffusion barriers (4.06 eV for W and 1.00 eV for Se) are considerably higher than those for adatom diffusion [60]. Compact domains are produced close to the adsorption–desorption equilibrium, in which the growth rate and $S_c$ are relatively low. Higher W flux not only leads to a higher growth rate and increased nucleation density, but also results in fractal shapes. The fractal structure may be undesirable since defects could be created along the rough edges as the domains grow [60]. In the time-dependent study of the growth process shown in figures 3(c) and (d), the transition from triangular shaped domains to fractal was also observed; this transition is associated with the expanded domains which capture more adatoms, breaking the equilibrium between attachment and edge diffusion. In addition to the triangular and fractal structures, 'nanorod' shaped grains are observed in the low-temperature growth regime (~350 °C) as shown in figure 4(j). Similar results of nanorod morphology have previously been reported in MBE-grown $WSe_2$ and $MoSe_2$ grown at low substrate temperature [10, 15, 69]. The nanorod structure has been speculated to be a significant deviation from the 2D growth scheme due to a local Se-deficient environment.

### 3.7. Chalcogen environment critical to promote larger grain 2D growth

As mentioned earlier, the chalcogen sticking coefficient is much lower than that of the transition metal due to the short mean lifetime and mean free path of the Se adatoms [60]. In a Se-poor environment, as shown in figure 5(a), pyramid-like grain morphology and particle protrusion features are observed in the center of grains (~5–10 nm in height shown in the supporting information figure S6). This contrasts with a Se-rich environment (figure 5(c)) where, for an identical growth time, bilayer $WSe_2$ with similar lateral grain size and no protrusion was achieved. The decrease in the protrusion features as a function of increasing Se flux suggests that the initial nuclei formed in the Se-deficient condition are W-rich, which is confirmed by the observation of W–W and $WO_x$ bonding in the XPS spectra in figure S7. Metal clustering with incomplete Se-passivation promotes the vertical growth of $WSe_2$, as illustrated in figure 5(b). Under a Se-rich condition, Se atoms limit the formation of W-rich nuclei and the covalent-bond-free surface of $WSe_2$ promotes lateral growth of the grain. This is clearly observed in figures 5(a) and (c) where a similar lateral grain size (~200 nm edge length) is observed for an 8-layer (Se-poor environment) and a bilayer film

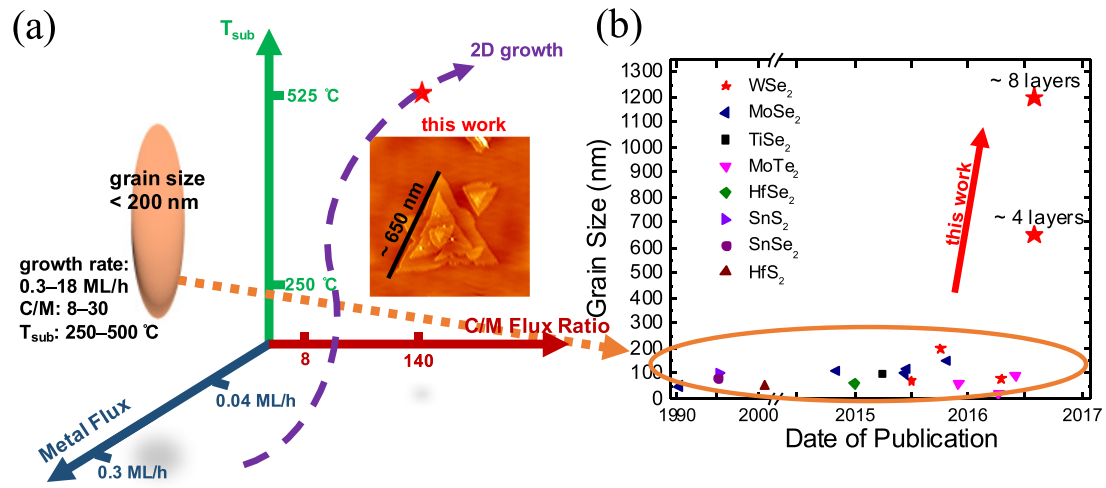


**Figure 6.** (a) Illustration of the experimental path (purple dash line) to achieve large grain size TMDs compared with the growth conditions (orange ellipsoid) utilized from prior reports with small grains. (Inset) AFM image of a 650 nm grain for 4-layer MBE-grown $WSe_2$ achieved in this study (red star) following this path. (b) Summary of the grain size of MBE grown TMDs reported in the literature along with the results achieved in this study. The data points used from previously published reports are either the grain sizes reported in the paper or from the longest linear dimension measured in a single grain in AFM or SEM images shown in those papers.

(Se-rich environment). First-principles based KMC simulations confirm that while monolayer growth is expected with sufficient Se supply, under chalcogen deficient growth conditions, metal clustering becomes more probable and strongly influences nucleation as shown in the supporting information. Additionally, this metal-rich clustering affects the critical nucleus size [59]. The critical nucleus size for tungsten metal is a $W_3$ trimer at 500 °C with a radius of 0.31 nm, which is nearly an order of magnitude smaller than the critical nucleus size of $WSe_2$. A Se-rich environment, on the other hand, reduces the probability of W–W bond formation, thus suppressing the formation of W clusters, resulting in the reduction of the nucleation density (figures 5(e)–(g)) and the aforementioned vertical growth promoting larger grain lateral growth.

### 3.8. Order of magnitude improvement in grain size and path to large area, scalable TMDs

The results of this nucleation and growth study indicate that to limit the nucleation density and promote 2D layered growth, it is necessary to have a low metal flux in conjunction with an elevated substrate temperature. At the same time, providing a Se-rich environment is important to suppress the formation of W-rich nuclei, which in turn suppresses vertical growth and promotes 2D growth. While these findings seem intuitive when presented in this systematic manner, it should be noted that growth parameters in those ranges have *not* been used historically. By combining these findings, we developed a strategy for the growth of large-area $WSe_2$ thin films as illustrated in figure 6(a). This strategy was then used to guide the growth of $WSe_2$ by MBE achieving layers with a grain size of ~1.2 $\mu$m (8 layers) and ~650 nm (4 layers), a drastic improvement over previously reported results as summarized in figure 6(b) from over 25 years of research [1–15]. Continuing along the path illustrated in figure 6(a) should enable large-area monolayer $WSe_2$ growth (limitations associated with the substrate heater design for the MBE system used for this work prevent going to the higher temperatures necessary to demonstrate large-area monolayer growth at this time).

While this work uses a van der Waals substrate and elemental precursors, the conclusions and mechanisms can be applied to an epitaxy system with increased complexity of both the substrate and precursors with minor modifications. For example, a stronger interaction between a non-van der Waals substrate and the precursors will limit the diffusion of the precursors causing the homogeneous nucleation density to increase. Higher impurity levels will also increase the heterogeneous nucleation density. Additionally, the breakdown of the molecular precursors in chemical vapor deposition (CVD) and metal-organic chemical vapor deposition (MOCVD) requires a high activation energy, slowing down the growth process [60–62]. All of these modifications result in a 'shifting' of the experimental conditions to a region of higher temperature and a higher flux (pressure), yet the underlying concepts remain the same as described throughout this work.

## 4. Conclusions

In this work, we have demonstrated that high quality $WSe_2$ can be grown using van der Waals epitaxy. Despite the large lattice mismatch with the substrate, the grown $WSe_2$ films have no misfit dislocations or strain and are rotationally aligned to the van der Waals substrates. The overwhelming in-plane bonding compared to the out-of-plane van der Waals interaction makes it unsuitable to use traditional growth mode terminology to describe the epitaxial growth of van der Waals materials like TMDs. Kinetic

issues such as low probability of Se incorporation, high metal–metal bonding strength, and non-equilibrium growth make it challenging to obtain 2D growth. However, our results indicate that lowering the W flux in conjunction with elevated substrate temperature reduces the nucleation density while providing a Se-rich environment is important to promote 2D growth. Using this growth strategy has enabled an increase of over one order of magnitude in grain size for $WSe_2$ compared to all previous TMD growth by MBE. The knowledge gained from this nucleation and growth study provides a roadmap toward large area TMD grains and potentially other van der Waals systems.

## Acknowledgments

This work is supported in part by the Center for Low Energy Systems Technology (LEAST), one of six centers supported by the STARnet phase of the Focus Center Research Program (FCRP), a Semiconductor Research Corporation program sponsored by MARCO and DARPA. It is also supported by the SWAN Center, a SRC center sponsored by the Nanoelectronics Research Initiative and NIST. This work was also supported in part by NSF Award No. 1407765 and the Texas Higher Education Coordinating Board's Norman Hackerman Advanced Research Program. JWPH acknowledges the support from Texas Instruments Distinguished Chair in Nanoelectronics. PRC acknowledges the financial support by the Leading Foreign Research Institute Recruitment Program through the National Research Foundation of Korea (NRF) funded by the Ministry of Science, ICT & Future Planning (MSIP) (2013K1A4A3055679). The authors also thank the Texas Advanced Computing Center (TACC) for providing computation resources.

## Supporting information

AFM spatial resolution discussion, structural and chemical characterization of $WSe_2$, experimentally determined band alignment of $WSe_2$, sticking coefficient calculations, detailed experimental parameter settings, AFM line profiles of $WSe_2$, and the impact of Se flux on XPS chemical states (PDF), two KMC simulation animations on $WSe_2$ critical nucleus size and metal clustering (GIF)

## Conflict of interest

The authors declare no competing financial interest.

## ORCID iDs

Chaoping Liang https://orcid.org/0000-0002-2910-2938

## References

[1] Ohuchi F S, Parkinson B A, Ueno K and Koma A 1990 *J. Appl. Phys.* **68** 2168–75
[2] Schlaf R, Louder D, Lang O, Pettenkofer C, Jaegermann W, Nebesny K W, Lee P A, Parkinson B A and Armstrong N R 1995 *J. Vac. Sci. Technol.* A **13** 1761–7
[3] Kreis C, Werth S, Adelung R, Kipp L, Skibowski M, Voss D, Kruger P, Mazur A and Pollmann J 2002 *Phys. Rev.* B **65** 153314
[4] Yue R Y *et al* 2015 *ACS Nano* **9** 474–80
[5] Ugeda M M *et al* 2014 *Nat. Mater.* **13** 1091–5
[6] Roy A *et al* 2016 *ACS Appl. Mater. Interfaces* **8** 7396–402
[7] Peng J P, Guan J Q, Zhang H M, Song C L, Wang L L, He K, Xue Q K and Ma X C 2015 *Phys. Rev.* B **91** 121113
[8] Vishwanath S *et al* 2015 *2D Mater.* **2** 024007
[9] Liu H J *et al* 2015 *2D Mater.* **2** 034004
[10] Jiao L *et al* 2015 *New J. Phys.* **17** 053023
[11] Diaz H C, Ma Y J, Chaghi R and Batzill M 2016 *Appl. Phys. Lett.* **108** 191606
[12] Diaz H C, Chaghi R, Ma Y J and Batzill M 2015 *2D Mater.* **2** 044010
[13] Zhang C, Chen Y, Johnson A, Li M-Y, Li L-J, Mende P C, Feenstra R M and Shih C-K 2015 *Nano Lett.* **15** 6494–500
[14] Park J H *et al* 2016 *ACS Nano* **10** 4258–67
[15] Jiao L 2015 *PhD Thesis* The University of Hong Kong
[16] Wang Q H, Kalantar-Zadeh K, Kis A, Coleman J N and Strano M S 2012 *Nat. Nanotechnol.* **7** 699–712
[17] Jaegermann W and Tributsch H 1988 *Prog. Surf. Sci.* **29** 1–167
[18] Chhowalla M, Shin H S, Eda G, Li L-J, Loh K P and Zhang H 2013 *Nat. Chem.* **5** 263–75
[19] Eichfeld S M *et al* 2015 *ACS Nano* **9** 2080–7
[20] Campbell P M, Tarasov A, Joiner C A, Tsai M Y, Pavlidis G, Graham S, Ready W J and Vogel E M 2016 *Nanoscale* **8** 2268–76
[21] Walsh L A *et al* 2017 *2D Mater.* **4** 025044
[22] Mak K F, Lee C, Hone J, Shan J and Heinz T F 2010 *Phys. Rev. Lett.* **105** 136805
[23] Splendiani A, Sun L, Zhang Y, Li T, Kim J, Chim C-Y, Galli G and Wang F 2010 *Nano Lett.* **10** 1271–5
[24] Li T and Galli G 2007 *J. Phys. Chem.* C **111** 16192–6
[25] Gong C, Zhang H, Wang W, Colombo L, Wallace R M and Cho K 2013 *Appl. Phys. Lett.* **103** 053513
[26] Koma A, Sunouchi K and Miyajima T 1984 *Microelectron. Eng.* **2** 129–36
[27] Ueno K, Abe H, Saiki K and Koma A 1991 *Japan. J. Appl. Phys.* **30** L1352
[28] Cui Y *et al* 2015 *Adv. Mater.* **27** 5230–4
[29] Aretouli K E, Tsoutsou D, Tsipas P, Marquez-Velasco J, Aminalragia Giamini S, Kelaidis N, Psycharis V and Dimoulas A 2016 *ACS Appl. Mater. Interfaces* **8** 23222–9
[30] Tonndorf P *et al* 2013 *Opt. Express* **21** 4908–16
[31] Kośmider K, González J W and Fernández-Rossier J 2013 *Phys. Rev.* B **88** 245436
[32] Jones A M *et al* 2013 *Nat. Nanotechnol.* **8** 634–8
[33] Shokouh S H H, Jeon P J, Pezeshki A, Choi K, Lee H S, Kim J S, Park E Y and Im S 2015 *Adv. Funct. Mater.* **25** 7208–14
[34] Liu W, Kang J H, Sarkar D, Khatami Y, Jena D and Banerjee K 2013 *Nano Lett.* **13** 1983–90
[35] Chuang H J *et al* 2014 *Nano Lett.* **14** 3594–601
[36] Roy T *et al* 2015 *ACS Nano* **9** 2071–9
[37] McDonnell S, Addou R, Buie C, Wallace R M and Hinkle C L 2014 *ACS Nano* **8** 2880–8
[38] Addou R *et al* 2015 *ACS Nano* **9** 9124–33
[39] Whangbo M H, Ren J, Magonov S N, Bengel H, Parkinson B A and Suna A 1995 *Surf. Sci.* **326** 311–26
[40] Addou R and Wallace R M 2016 *ACS Appl. Mater. Interfaces* **8** 26400–6
[41] Wallace R M 2014 *ECS Trans.* **64** 109–16
[42] Horcas I, Fernandez R, Gomez-Rodriguez J M, Colchero J, Gomez-Herrero J and Baro A M 2007 *Rev. Sci. Instrum.* **78** 013705

[43] Kresse G and Joubert D 1999 *Phys. Rev.* B **59** 1758–75
[44] Perdew J P, Burke K and Ernzerhof M 1996 *Phys. Rev. Lett* **77** 3865–8
[45] Kresse G and Joubert D 1996 *Phys. Rev.* B **54** 11169–86
[46] Henkelman G, Uberuaga B P and Jónsson H 2000 *J. Chem. Phys.* **113** 9901–4
[47] Henkelman G and Jónsson H 2000 *J. Chem. Phys.* **113** 9978–85
[48] Nie Y, Liang C, Cha P-R, Colombo L, Wallace R M and Cho K 2017 *Sci. Rep.* **7** 2977
[49] Brixner L H 1962 *J. Inorg. Nucl. Chem.* **24** 257–63
[50] Lin Y C *et al* 2015 *Nat. Commun.* **6** 7311
[51] Schlaf R, Armstrong N R, Parkinson B A, Pettenkofer C and Jaegermann W 1997 *Surf. Sci.* **385** 1–14
[52] Ohuchi F S, Shimada T, Parkinson B A, Ueno K and Koma A 1991 *J. Cryst. Growth* **111** 1033–7
[53] Kalikhman V and Umanskiĭ Y S 1973 *Sov. Phys.—Usp.* **15** 728
[54] Cheng J X *et al* 2015 *Adv. Mater.* **27** 4069–74
[55] Ago H, Fukamachi S, Endo H, Solis-Fernandez P, Yunus R M, Uchida Y, Panchal V, Kazakova O and Tsuji M 2016 *ACS Nano* **10** 3233–40
[56] Lee G *et al* 2009 *ECS Trans.* **19** 185–99
[57] Tarasov A, Campbell P M, Tsai M Y, Hesabi Z R, Feirer J, Graham S, Ready W J and Vogel E M 2014 *Adv. Funct. Mater.* **24** 6389–400
[58] Saidi W A 2014 *Cryst. Growth Des.* **14** 4920–8
[59] Michely T and Krug J 2004 *Islands, Mounds, and Atoms: Patterns and Processes in Crystal Growth Far from Equilibrium* (Berlin: Springer)
[60] Nie Y F *et al* 2016 *2D Mater.* **3** 025029
[61] Lin K-H, Wang S-L, Chen C and Ju S-P 2014 *RSC Adv.* **4** 24286–94
[62] Pan B C, Han J G, Yang J and Yang S 2000 *Phys. Rev.* B **62** 17026–30
[63] Cacciuto A and Frenkel D 2005 *J. Phys. Chem.* B **109** 6587–94
[64] Brune H 1998 *Surf. Sci. Rep.* **31** 121–229
[65] Gu S L, Zheng Y D, Zhang R, Wang R H and Zhong P X 1994 *J. Appl. Phys.* **75** 5382–4
[66] Foxon C T and Joyce B A 1975 *Surf. Sci.* **50** 434–50
[67] Kaur I, Pandya D K and Chopra K L 1980 *J. Electrochem. Soc.* **127** 943–8
[68] Bales G S and Chrzan D C 1995 *Phys. Rev. Lett.* **74** 4879–82
[69] Lehtinen O *et al* 2015 *ACS Nano* **9** 3274–83